Mantle structure and flow across the continent-ocean transition of the eastern North American margin: anisotropic *S*-wave tomography

Brennan R. Brunsvik[1] *, Zachary C. Eilon[1], Colton Lynner[2]

[1]Department of Earth Science, University of California, Santa Barbara, CA, USA

[2]Department of Earth Science, University of Delaware, Newark, DE, USA

Contents of this file

1. Sections S1 to S7. Section S1: Multi-channel cross-correlation. Section S1.1: Delay time datasets, processing, and quality control. Section S1.2: Dependence of MCCC on particle motion polarization. Section S2: Tomography parameterization. Section S3: Crustal corrections and static terms. Section S4: Finite frequency approximation. Section S5: Regularization. Section S6: Spike test. Section S7: Squeezing test.

2. Figures S1 to S16. Figure S1: Comparison of shear-wave splitting fast polarizations to assumed anisotropic geometry. Figure S2: Crustal corrections for splitting and differential travel times. Figure S3: L-tests for regularization parameters. Figure S4: Depth-slice

*Department of Earth Science, Webb Hall, University of California, Santa Barbara, CA 93106

of model where anisotropy is permitted at all depths. Figure S5: Cross-section of model where anisotropy is permitted at all depths. Figure S6: Synthetic splitting example showing split and splitting corrected waveforms and transverse energy surface. Figure S7: Multi-channel cross-correlation example, showing pre- and post-corrected waveforms and particle motion. Figure S8: Splitting and differential travel times averaged at each station. Figure S9: Velocity checkerboard tests. Figure S10: Anisotropy checkerboard tests. Figure S11: Velocity spike test. Figure S12: Anisotropy spike test. Figure S13: Squeezing test. Figure S14: Synthetic input-output test evaluating specific velocity features. Figure S15: Synthetic input-output test evaluating specific anisotropy features. Figure S16: Velocity and anisotropy models in 3-D.

Additional Supporting Information (Files uploaded separately)

1. Description of interactive tomography model file `brunsvik-tomog.html`

Introduction

This supporting document contains details and figures regarding multi-channel cross-correlation and tomography, as well as tests for resolution, regularization, and for synthetic splitting predictions using a ray-based approach. We included an interactive tomography model figure as `brunsvik-tomog.html`.

S1. Multi-channel cross-correlation

We used multi-channel cross-correlation (MCCC) to measure splitting and differential travel times (VanDecar & Crosson, 1990). Traditionally, travel time differences between each pair of stations are measured through cross-correlation to produce the data vector $\mathbf{d}$. These delay times constitute the model vector $\mathbf{m}$, which are self-consistent differential travel times we seek. These vectors are linearly related through $\mathbf{Gm} = \mathbf{d}$. Differential

travel times are inverted using weighted least squares. The additional steps we employ to jointly measure splitting with differential travel times is described in Section 2.1 and Eilon, Abers, and Gaherty (2016).

S1.1. Delay time datasets, processing, and quality control

The seismic array we use has a total aperture of $\sim$ 1500 km east-west and $\sim$ 1000 km north-south. We used shear-wave arrivals from earthquakes between 30° and 151°. We used a distance-dependent M_W cutoff to select events for processing. The minimum M_W cutoff varies linearly between $M_W > 5.5$ at a distance of 30° to $M_W > 6.5$ for events at 135° (*e.g.,* Liu & Gao, 2018). This gives 2326 candidate earthquakes.

We collected splitting and differential travel time datasets from a combination of novel measurements and previously published data. First, we measured differential travel times and splitting times at all stations in our meta-array. We retained splitting times in the coastal region, but discarded these and used only the differential travel times over a wider region (Figure S1 and 2). In addition to this dataset, we processed OBSs a second time, primarily to reduce sparsity of OBS data. For this second dataset, we did not reject waveforms automatically. We manually inspected and considered all waveforms to ensure that signals with good quality were not rejected. Still, due to a shorter deployment interval and a noisier station environment, we obtained fewer travel time and splitting measurements at offshore stations than onshore. To account for this difference in data power within the inversion, we upweighted all OBS measurements by a compensating factor (3x) in the tomography. Third, we incorporated *SK(K)S-PKS* splitting measurements from the literature in our anisotropic region (Figure 1), which were measured using standard splitting techniques (Long et al., 2016; Lynner & Bodmer, 2017; Yang et al., 2017).

We applied the following quality control and data processing prior to MCCC inversions. We removed instrument responses and rotated OBSs to north and east using instrument orientations measured from surface wave polarizations (Lynner & Bodmer, 2017). We rejected body wave arrivals with signal-to-noise ratios less than 2.8 for land stations or 2 for OBSs. We removed phase arrivals which had less than $\sim$ 10 s of separation from another phase. For arrivals with strongly non-linear particle motion, we found our splitting measurements unreliable. Elliptical particle motion for one earthquake's phase arrival, stacked across the array, could also indicate strong source-side splitting. We excluded earthquakes with particle motion ellipticity on the stacked waveform > 0.33. We chose this number by visually inspecting the splitting corrected waveforms for quality, in particular, the similarity and alignment of the splitting corrected S-pulses. We defined ellipticity as the ratio of minimum to maximum eigenvalues of the horizontal particle motion covariance matrix (*e.g.,* Silver & Chan, 1991). We applied a Butterworth band pass filter with high- and low-pass frequencies hand-selected for each earthquake to maximize clarity of the pulse while retaining high frequency energy. The average low- and high-pass frequencies were 0.129 Hz and 0.031 Hz, respectively. After applying MCCC, we rejected measurements which exhibited cycle skipping, had a cross-correlation coefficient with the waveform stack of less than 0.55 for land stations or 0.4 for OBSs, or had increased ellipticity of particle motion. We also rejected waveforms with visually dissimilar pulse shapes or which maintained misalignment of the pulses after applying MCCC.

S1.2. Dependence of MCCC on particle motion polarization

The occurrence of detectable splitting depends on the particle motion polarization relative to the anisotropic symmetry axis. We assume a symmetry axis parallel to $\phi = \text{N33°E}$.

Where particle motion is parallel or perpendicular to ϕ, we expect no splitting. For S-wave arrivals with mean polarization measured to be within 22.5° of ϕ, we used the standard MCCC process to measure only $\delta T_{\parallel}$, the differential travel times at all stations for quasi-S waves polarized parallel to the margin. Similarly, for S-wave arrivals with mean polarization measured to be less than 22.5° from the perpendicular to ϕ, we measured only $\delta T_{\perp}$. Where particle motion polarization is between 22.5° and 67.5° from ϕ, splitting may occur. In this case, we used cross-correlation between each station pair allowing us to measure both $\delta T_{\perp}$ and $\delta T_{\parallel}$. At each individual station, we cross-correlated the margin-parallel and margin-perpendicular horizontal components to measure the splitting times dT_{splt} at each station (Eilon et al., 2016). The resulting quasi-shear wave splitting and differential travel times become the data inputs for our tomographic inversion.

S2. Tomography parameterization

We followed the methodology of Eilon et al. (2016) in applying several key assumptions to reduce the number of independent elastic tensor parameters to two. First, we assume a hexagonal elastic tensor with horizontal symmetry axis of fixed orientation throughout the model to simplify the elastic tensor to 5 independent parameters from 23 (21 elastic and 2 orientation parameters). As noted in Section 2.2, the fixed symmetry axis is not equivalent to assuming a fixed fast orientation, and the assumption is justified by observations of simple splitting from SKS data. Under this parameterization, a shear wave with vertical incidence is already fully described by $V_{\parallel}$ and $V_{\perp}$. By assuming that the anisotropic parameter $\eta = 1$, $V_{P_{av}} = \nu V_{S_{av}}$ where $\nu = 1.8$, and that P and S anisotropy are equal, the elastic tensor can be parameterized as a function of only two values, $V_{\parallel}$ and $V_{\perp}$, for arbitrarily incident rays.

For a ray propagating at an angle ζ to the horizontal hexagonal symmetry axis, the two quasi-shear wave velocities that result from the Christoffel equations are V_{SH} and V_{SV}. V_{SH} is always perpendicular to the hexagonal symmetry axis and is precisely calculable on the basis of $V_{\parallel}$ and $V_{\perp}$. V_{SV} is more complex. We assume the V_{SV} wave is polarized in the vertical plane, which contains the ray propagation path (Eilon et al., 2016). The wavespeed, V_{SV}, is then approximated by a function varying symmetrically about $\zeta = 45°$ between 0° and 90°. The error associated with this assumption is small and discussed in Eilon et al. (2016). The quasi-shear wave velocities are thus:

$$V_{SH}(\zeta) = \sqrt{V_{\perp}^2 \sin^2 \zeta + V_{\parallel}^2 \cos^2 \zeta}$$

$$V_{SV}(\zeta) \approx \sqrt{V_{\parallel}^2 \cos^2 2\zeta + \left(\nu^2 \left[V_{\parallel}^2 - V_{\perp}^2\right]/4 + V_{\parallel}^2\right) \sin^2 2\zeta}$$

Based on our assumptions, Vsh and Vsv correspond directly to the two split quasi-S wave velocities. This paramaterization achieves two key goals: 1) The assumption of fixed symmetry axis makes the splitting process straightforwardly additive (rather than strongly non-commutative). 2) These expressions allow for analytical differentiation of delay times with respect to model parameters. This enables efficient utilization of Newton's method to solve the non-linear inversion.

S3. Crustal corrections and static terms

The relationship between data and model involves integrating slowness through the model, accounting for event and station static terms, and applying a crustal correction. The model is $\mathbf{m} = \left\{\mathbf{V}_{\perp}, \mathbf{V}_{\parallel}, \delta\mathbf{T}_{\mathrm{evt}}, \delta\mathbf{T}_{\mathrm{sta}}, \mathbf{dT}_{\mathrm{evt}}, \mathbf{dT}_{\mathrm{sta}}\right\}$ which is related to data as $\mathbf{d} = g(\mathbf{m}) + \delta\mathbf{T}_{crust}$ (these terms are defined below) (Eilon et al., 2016). Note that the symbol δ corresponds to isotropic travel times and d to splitting times.

We applied *a priori* crustal corrections $\delta\mathbf{T}_{\text{crust}}$ to account for the influence of known crustal heterogeneity on delay times (Figure S2; *e.g.,* Sandoval et al., 2004). We remove the travel times which deviate from those of a mean crust with thickness $h = 39$ km and $Vs = 3.5$ km/s. We adjust arrival times of all stations to account for elevation, correcting to sea level. We use the crustal velocity and depth model of Shen and Ritzwoller (2016) for the continental crust and Shuck, Van Avendonk, and Bécel (2019) for the oceanic crust. The crustal corrections, ray-averaged at each station, can be seen in Figure S2.

Shallow structure is not formally resolvable using body wave tomography, given the average station spacing of about 70 km. To account for error in *a priori* crustal correction terms, or stations for which crustal values are not independently constrained, we also solved for damped station static travel time terms $\delta\mathbf{T}_{\text{sta}}$ and event travel time terms $\delta\mathbf{T}_{\text{evt}}$. Direct S phase source splitting can be several seconds and contaminate our anisotropy model. This is solved for as event splitting static terms $\mathbf{dT}_{\text{evt}}$. Source-side splitting is thus parsed out separately from splitting in the mantle anisotropy model. Station static splitting terms $\mathbf{dT}_{\text{sta}}$ account for anisotropy that is too shallow to resolve in the main model.

S4. Finite frequency approximation

We account for finite frequency effects using simplified, ray-based kernels (Schmandt & Humphreys, 2010). First, we conduct ray tracing using the reference IASP91 1-D velocity model (Kennett & Engdahl, 1991). Each travel time was calculated using $\delta t = \iiint_{\oplus} K(\mathbf{x})/\delta v\,(\mathbf{x})\, d^3\mathbf{x}$ where $K(\mathbf{x})$ is the sensitivity kernel and δv is the perturbational velocity (δv depends on anisotropy as described in Section S2). We use a modified version of Eq. 2 from Schmandt and Humphreys (2010) to approximate the sensitivity kernel

$K(\mathbf{x})$, ignoring the region outside the first Fresnel zone:

$$K(R_N) \approx A \frac{\sin\left(\pi\left(\frac{R_N}{R_{F_1}(D_R, D_{Rmax}, f_c)}\right)^2\right)}{\int_0^{R_N}\int_0^{2\pi} \sin\left(\pi\left(\frac{R_N}{R_{F_1}(D_R, D_{Rmax}, f_c)}\right)^2\right) d\theta dR_N} \tag{1}$$

where R_N is the ray-normal distance, R_{F_1} is the first Fresnel zone radius, D_R is along-ray distance, D_{Rmax} is the total ray length, and f_c is the center frequency used when cross-correlating waveforms. The denominator involves an integral in the plane normal to the ray. For a given ray, the denominator varies only as a function of D_R. The denominator scales the sensitivity along D_R to account for increase in R_{F_1} with D_R.

Similar to Schmandt and Humphreys (2010), we calculate A by assuming equivalence of travel time sensitivity using both ray and finite frequency approaches: $\iiint_{\oplus} K(\mathbf{x})/v_{ref}(\mathbf{x}) d^3\mathbf{x} = \int \frac{1}{v_{ref}(D_R)} dD_R$ where v_{ref} is the 1-D reference velocity. For calculating A, we only perform the integrals in the volume and along the ray corresponding to the portion of the ray where R_{F1} is contained completely within our model.

We approximate the first fresnel zone radius by assuming that all energy is contained at the center frequency f_c and that ray bending is insignificant. Then, the first Fresnel zone (*i.e.* the ray normal distance such that a reflector will cause a ray to arrive at a station with π phase lag compared to the direct ray) is:

$$R_{F_1} \approx \sqrt{\frac{v}{f_c} \frac{D_R\left(D_{Rmax} - D_R\right)}{D_{Rmax}}} \tag{2}$$

S5. Regularization

We conducted L-tests, which aid in determining the optimal model length penalty weight (ϵ) and second derivative roughness penalty weight (γ). We grid searched possible values of ϵ and γ and chose $\epsilon = 22$ and $\gamma = 4.2$ to minimize a regularization penalty function

$P(\epsilon, \gamma)$ (Figure S3). P is a linear combination of roughness, model norm, and data residual. We gave relative penalty weights to model length $\|\mathbf{m}(\epsilon, \gamma)\|$ and roughness $\|\mathbf{m}''(\epsilon, \gamma)\|$ using

$$A = (1 - 0.2)\|\mathbf{m}\| + 0.2\|\mathbf{m}''\|$$

We accounted for data misfit using

$$B = 1 - \mathrm{vr_w}$$

where $\mathrm{vr_w}$ is weighted variance reduction. Then, we calculated the final penalty as

$$P = (1 - 0.35)\left(\frac{A - min(A)}{max(A) - min(A)}\right) + 0.35\left(\frac{B - min(B)}{max(B) - min(B)}\right)$$

We also evaluated P when considering independently the splitting times/anisotropy model, or the differential travel times/isotropic velocity model (not reported here for brevity). We accordingly decreased anisotropy damping by 25% and increased anisotropy smoothing by 150% relative to velocity.

S6. Spike tests

Spike tests (Figure S11 and S12) indicate resolution and have a valuable mathematical meaning (Rawlinson & Spakman, 2016). They provide insight into the model resolution matrix, $\mathbf{R}$, whose rows can be thought of as the impulse response function of the inversion (Menke, 2012). Each row of $\mathbf{R}$ thus indicates the influence of one "true" model parameter on each inverted model parameter. Because it is often computationally infeasible to calculate the full resolution matrix, a spike test – using an input model that is zero at all nodes except for node i – is often used as a proxy for row i of $\mathbf{R}$. Note that in practice we must use a box-car or small spherical input rather than a true delta spike (*e.g.,* Rickers et al., 2013). The results of this test are described in Section 3.2.

S7. Squeezing test

We conducted a squeezing test to assess the depth extent which the data require significant velocity heterogeneity and anisotropy. We ran the tomographic inversion with the constraint that dVs and anisotropy are 0 beneath some squeezing depth, z_{sqz} (Figure S13). We varied this squeezing depth parameter, evaluating how variance reduction and model norm changed as a quantitative metric for the depth range over which our data *require* model structure. Variance reduction of delay times is a metric for consistency of the model with the data. Note that differential travel times correspond primarily to isotropic velocity, and splitting times correspond to anisotropy.

Differential travel time variance reduction continues to increase significantly as the squeezing depth increases, to $z_{sqz} \geq$ 1080km. This suggests the data require velocity heterogeneity to the 1080 km base of the model. Previous body wave tomography models suggest that structures associated with delamination, convection, sinking slabs, or other processes extend to similar depths (*e.g.,* Golos et al., 2018). Since our focus is on tectonics and mantle-plate dynamics, we do not interpret structures deeper than 660 km.

Splitting time variance reduction continues to increase as z_{sqz} increases. However, this gradient is modest. This suggests the splitting data do not strictly require deep structure. However, the anisotropy model norm increases with increasing z_{sqz}. With unsqueezed anisotropy, deep anisotropy magnitude matches shallow anisotropy magnitude (Figure S4 and S5). We interpret that splitting measurement error is mapped toward the base of the model if not squeezed. Differential travel measurements will also be partially mapped to the deep anisotropy model due to trade-off between anisotropy and velocity. The squeezing test corroborates our decision to permanently squeeze the anisotropy model to

what we *a priori* believe is the maximum likely anisotropy depth: 300 km (Chang et al., 2015).

File brunsvik-tomog.html Three dimensional view of anisotropy and velocity model; same as Figure S16. dVs isosurfaces are at $\pm 1.2\%, \pm 2.2\%$. Anisotropy isosurfaces are at $\pm 0.5\%, \pm 1.0\%$. Model only plotted where hit quality > 0.7. Moho adapted from Shen and Ritzwoller (2016) and Shuck et al. (2019). Simply open this file in a web browser to view. Turn on and off different layers (anisotropy, velocity, Moho, and topography) by clicking on their labels.

References

Chang, S., Ferreira, A. M. G., Ritsema, J., van Heijst, H. J., & Woodhouse, J. H. (2015). Joint inversion for global isotropic and radially anisotropic mantle structure including crustal thickness perturbations. *Journal of Geophysical Research: Solid Earth*, *120*(6), 4278–4300. doi: 10.1002/2014JB011824

Eilon, Z., Abers, G. A., & Gaherty, J. B. (2016). A joint inversion for shear velocity and anisotropy: The Woodlark Rift, Papua New Guinea. *Geophysical Journal International*, *206*(2), 807–824. doi: 10.1093/gji/ggw177

Golos, E. M., Fang, H., Yao, H., Zhang, H., Burdick, S., Vernon, F., ... van der Hilst, R. D. (2018). Shear Wave Tomography Beneath the United States Using a Joint Inversion of Surface and Body Waves. *Journal of Geophysical Research: Solid Earth*, *123*(6), 5169–5189. doi: 10.1029/2017JB014894

Kennett, B. L. N., & Engdahl, E. R. (1991). Traveltimes for global earthquake location and phase identification. *Geophysical Journal International*, *105*(2), 429–465. doi: 10.1111/j.1365-246X.1991.tb06724.x

Liu, L., & Gao, S. S. (2018). Lithospheric layering beneath the contiguous United States constrained by S-to-P receiver functions. *Earth and Planetary Science Letters*, *495*(1), 79–86. doi: 10.1016/j.epsl.2018.05.012

Long, M. D., Jackson, K. G., & McNamara, J. F. (2016). SKS splitting beneath Transportable Array stations in eastern North America and the signature of past lithospheric deformation. *Geochemistry, Geophysics, Geosystems*, *17*(1), 2–15. doi: 10.1002/2015GC006088

Lynner, C., & Bodmer, M. (2017). Mantle flow along the eastern North American margin inferred from shear wave splitting. *Geology*, *45*(10), 867–870. doi: 10.1130/G38980.1

Menke, W. (2012). *Geophysical Data Analysis: Discrete Inverse Theory* (3rd ed.). Elsevier. doi: 10.1016/C2011-0-69765-0

Rawlinson, N., & Spakman, W. (2016). On the use of sensitivity tests in seismic tomography. *Geophysical Journal International*, *205*, 1221–1243. doi: 10.1093/gji/ggw084

Rickers, F., Fichtner, A., & Trampert, J. (2013). The Iceland-Jan Mayen plume system and its impact on mantle dynamics in the North Atlantic region: Evidence from full-waveform inversion. *Earth and Planetary Science Letters*, *367*, 39–51. doi: 10.1016/j.epsl.2013.02.022

Sandoval, S., Kissling, E., Ansorge, J., & SVEKALAPKO Seismic Tomography working Group. (2004). High-resolution body wave tomography beneath the SVEKALAPKO array - II. Anomalous upper mantle structure beneath the central Baltic Shield. *Geophysical Journal International*, *157*(1), 200–214. doi: 10.1111/j.1365-246X.2004.02131.x

Schmandt, B., & Humphreys, E. (2010). Seismic heterogeneity and small-scale convection

in the southern California upper mantle. *Geochemistry, Geophysics, Geosystems*, *11*(5), 1–19. doi: 10.1029/2010GC003042

Shen, W., & Ritzwoller, M. H. (2016). Crustal and uppermost mantle structure beneath the United States. *Journal of Geophysical Research: Solid Earth*, *121*(6), 4306–4342. doi: 10.1002/2016JB012887

Shuck, B. D., Van Avendonk, H. J., & Bécel, A. (2019). The role of mantle melts in the transition from rifting to seafloor spreading offshore eastern North America. *Earth and Planetary Science Letters*, *525*, 115756. doi: 10.1016/j.epsl.2019.115756

Silver, P. G., & Chan, W. W. (1991). Shear wave splitting and subcontinental mantle deformation. *Journal of Geophysical Research*, *96*(B10), 16429–16454. doi: 10.1029/91jb00899

VanDecar, J. C., & Crosson, R. S. (1990). Determination of teleseismic relative phase arrival times using multi-channel cross-correlation and least squares. *Bulletin of the Seismological Society of America*, *80*(1), 150–169.

Yang, B. B., Liu, Y., Dahm, H., Liu, K. H., & Gao, S. S. (2017). Seismic azimuthal anisotropy beneath the eastern United States and its geodynamic implications. *Geophysical Research Letters*, *44*(6), 2670–2678. doi: 10.1002/2016GL071227

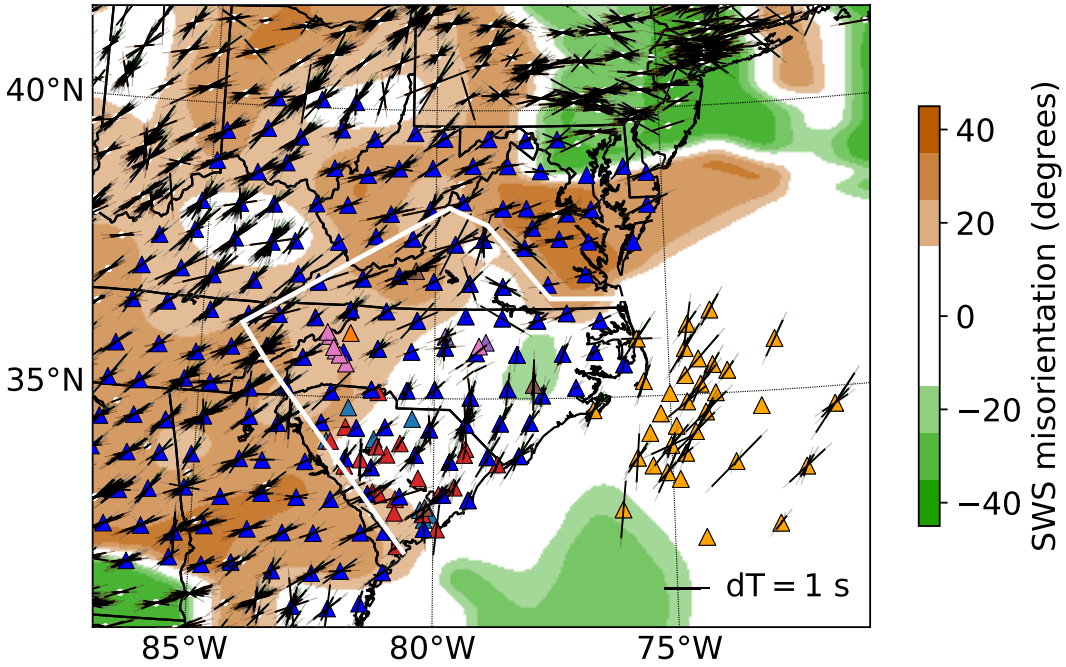

Figure S1. This shows the stations we use (triangles) and previous splitting measurements. The 30 OBSs and 3 land stations that were deployed as part of the ENAM-CSE are shown in orange. Dark blue triangles are the Transportable Array (TA). Other triangles are other networks. The white line shows the boundary between stations used for splitting and stations used only for delay times. Splitting delay times and orientations at OBSs (Lynner & Bodmer, 2017) and land stations (Long et al., 2016; Yang et al., 2017) are shown as black lines. Colors and contours illustrate mismatch between splitting measurements from the literature and the best matching quasi-S wave polarization predicted from our assumed hexagonal symmetry axis orientation (*i.e.* N33°E +n90°). The mismatch thus varies only between $-45°$ and 45° as it is equally acceptable for fast axes to be parallel or perpendicular to the symmetry axis, but our assumptions break down for mismatch of 45°. This mismatch is interpolated onto a grid using a Gaussian filter. A white contour is drawn roughly at 25° mismatch, which we use to limit the bounds of stations used for measuring splitting. OBS: ocean-bottom seismometer. ENAM-CSE: Eastern North American margin community seismic experiment.

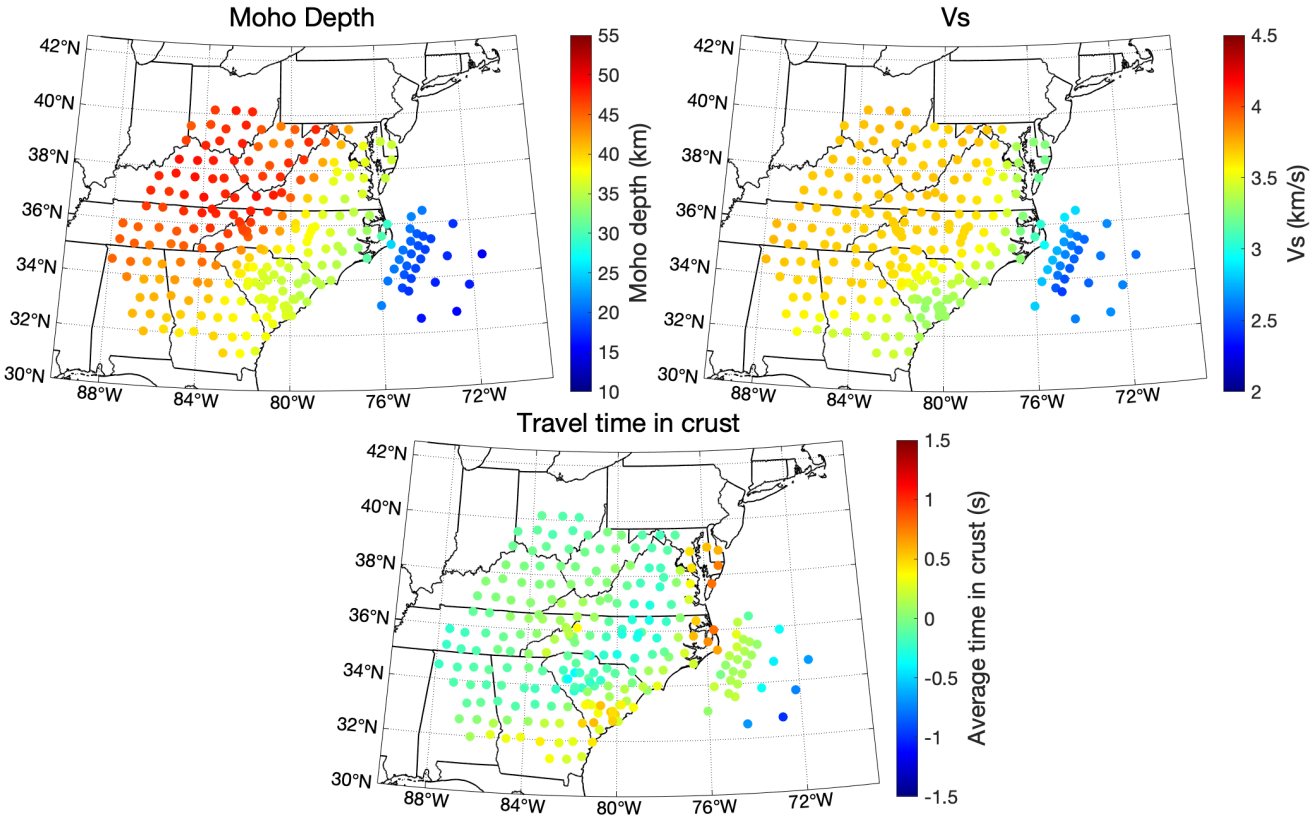

Figure S2. Crustal values and corrections which are applied to the differential travel time data. Top left shows Moho depth and right shows crustal velocity, which is used to calculate crustal corrections. The velocity and Moho profiles of Shen and Ritzwoller (2016) and Shuck et al. (2019) are used for the continental and oceanic crust, respectively. Bottom shows calculated crustal travel time in excess of what would be spent in a laterally homogenous crust. The plots show averages at each station. These values are *removed* from differential travel times to perform the crustal correction.

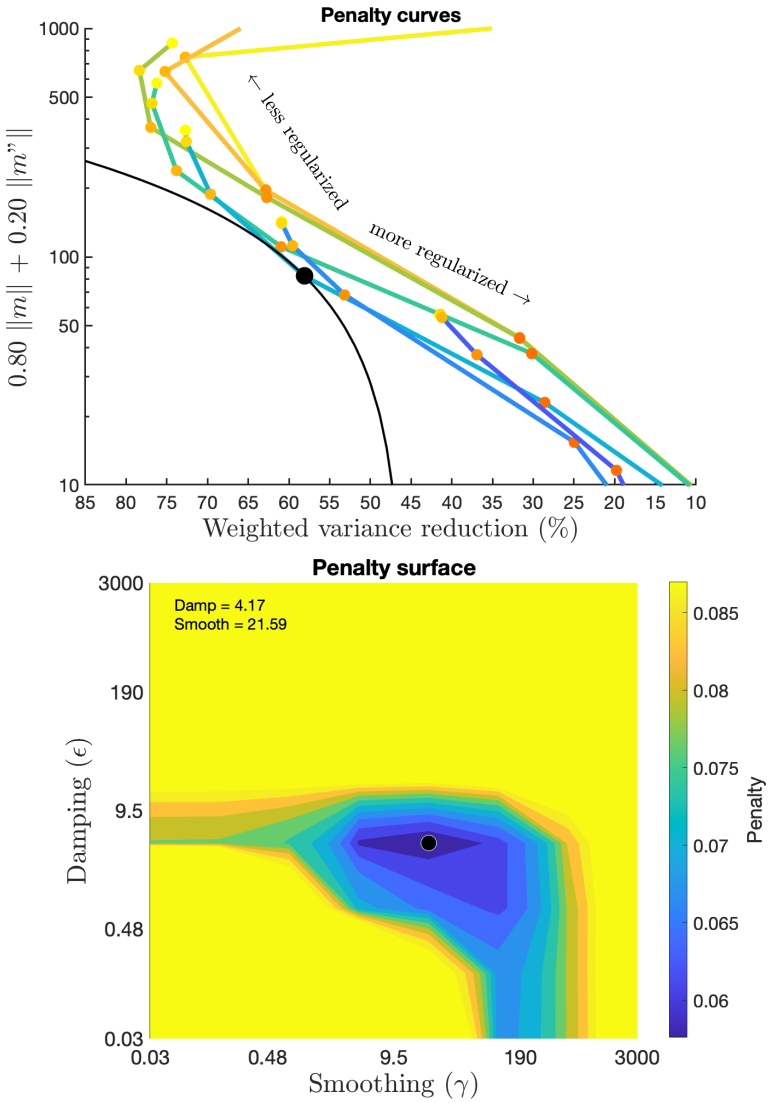

Figure S3. L-test used to determine the appropriate regularization parameters ϵ and γ for damping and second derivative smoothing respectively. The chosen values $\epsilon = 4.2$ and $\gamma = 22$ are plotted as black dots. (Top) Lines of constant γ and varied ϵ, showing linear combination of roughness and norm versus the consequent variance reduction. The black line delineates the maximum trade-off between norm/roughness and variance reduction. (Bottom) Surface showing the penalty (linear combination of model norm, roughness, and residual) associated with each set of ϵ and γ.

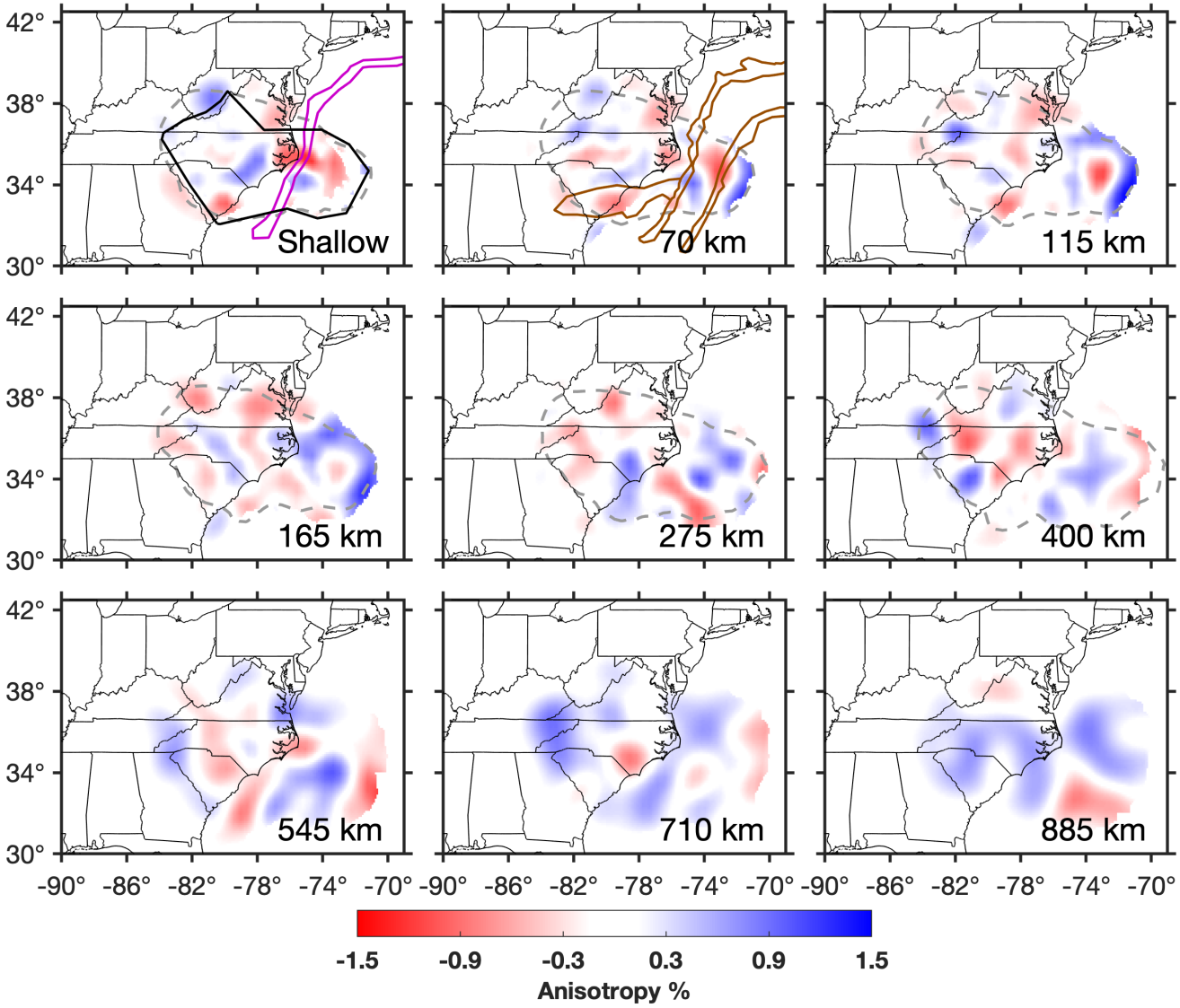

Figure S4. Model where anisotropy was permitted at all depths. See Figure 4 for more description.

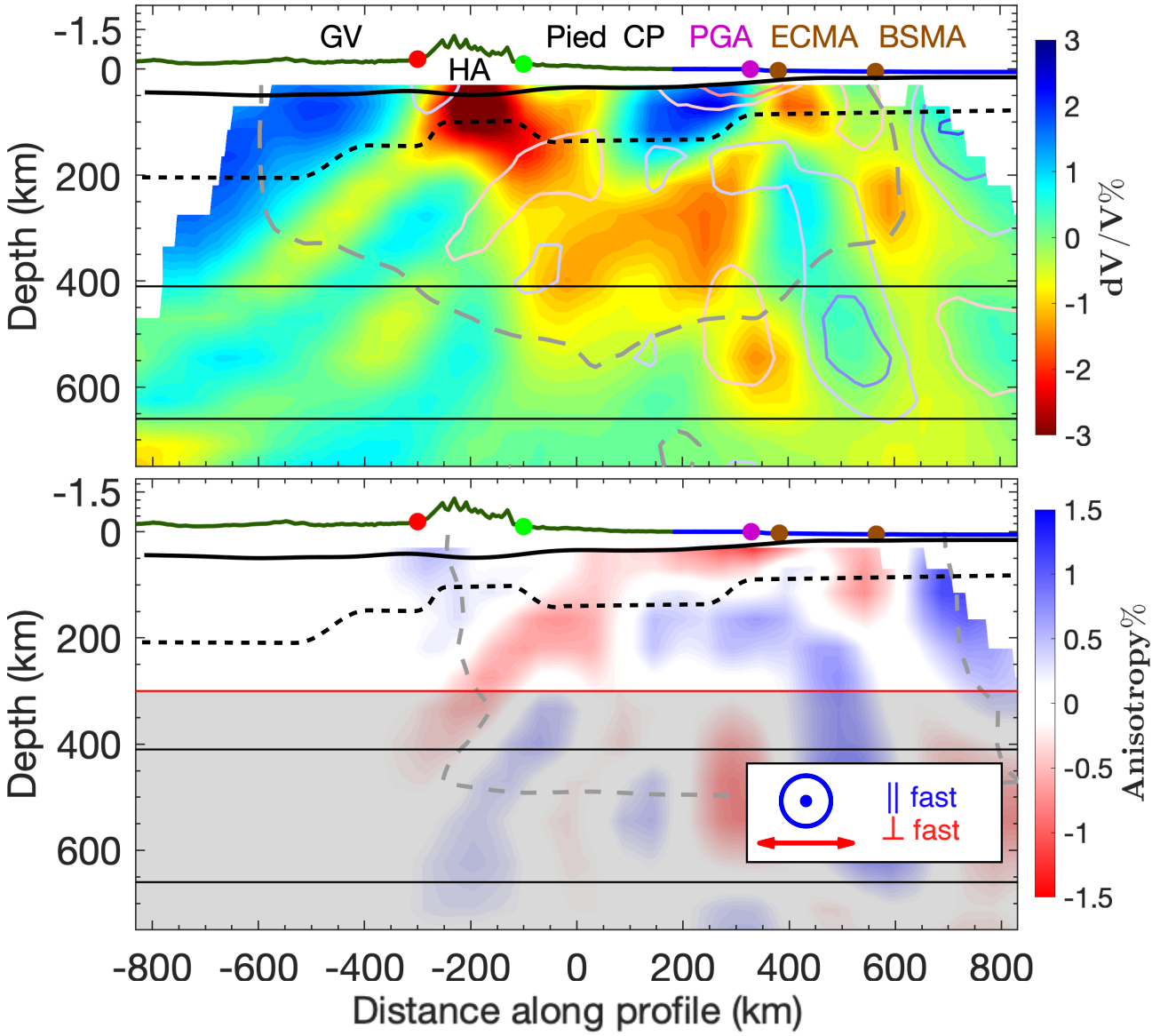

Figure S5. Model where anisotropy was permitted at all depths. See Figure 5 for more description.

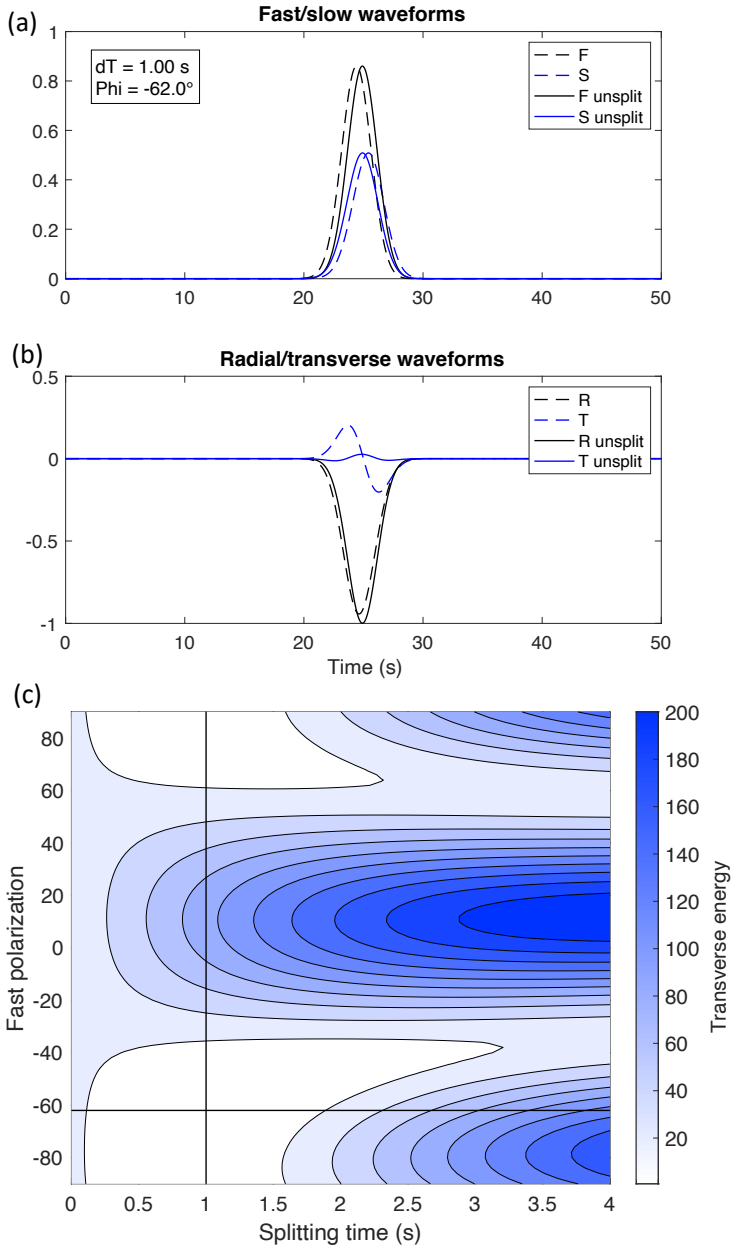

Figure S6. Results of synthetic splitting applied and measured by propagating a Gaussian pulse through the final inverted velocity and anisotropy model. (a) Split and splitting corrected fast (F) and slow (S) polarization components. (b) Split and splitting corrected radial (R) and transverse (T) components. (c) Transverse energy remaining after correcting for splitting. The location of minimum energy, which is plotted with a cross, indicates the splitting time and fast polarization.

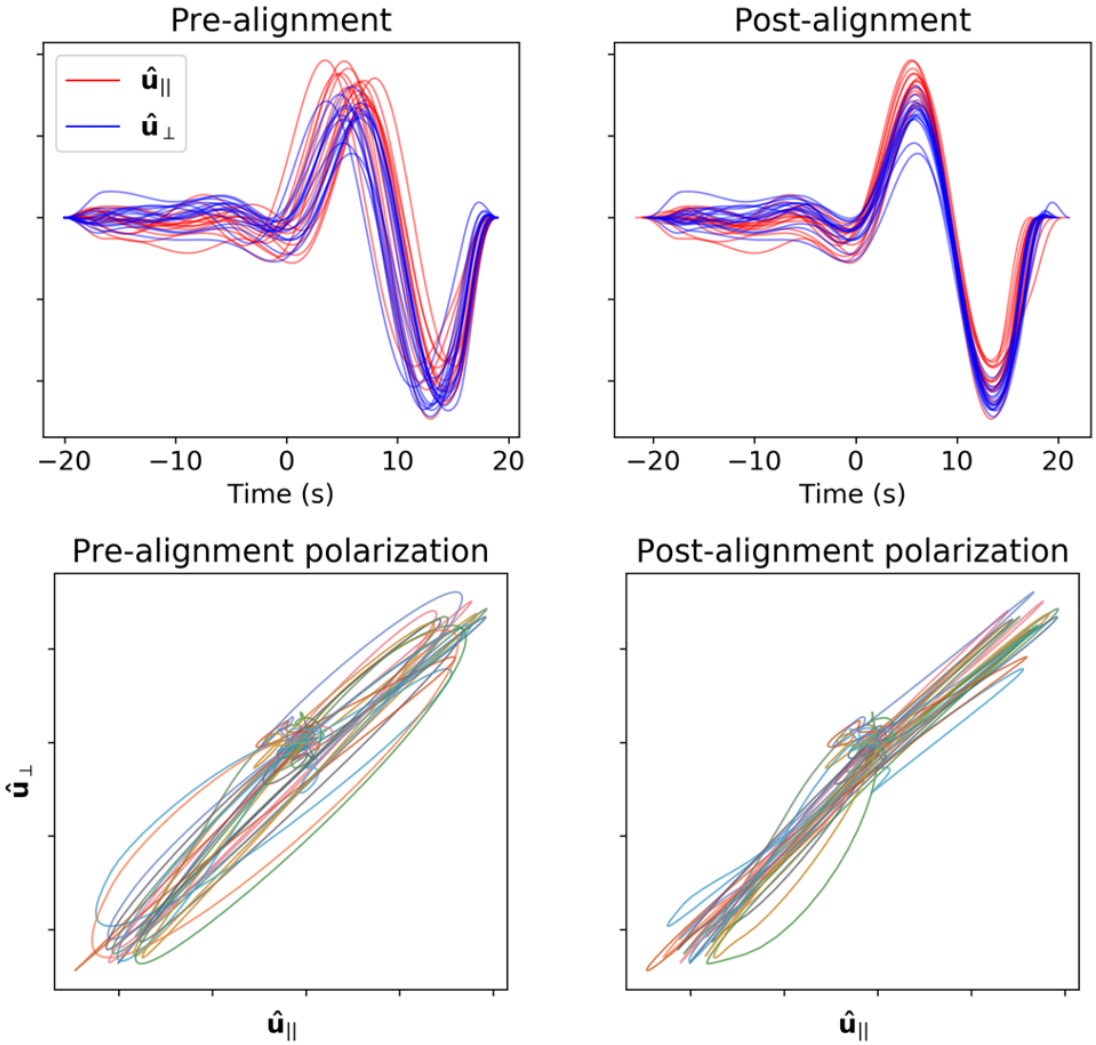

Figure S7. An example of our MCCC results. One earthquake's arrival at several stations are simultaneously plotted. The seismograms are rotated to have one component parallel to the anisotropic symmetry axis, $\mathbf{u}_{\parallel}$, and the other component perpendicular, $\mathbf{u}_{\perp}$. On the left, the waveforms are aligned by their arrival times predicted from a 1-D velocity model. On the right, results are shifted according to the MCCC inverted differential travel times and splitting times. The top shows waveforms. The bottom shows particle motions, with each color corresponding to a different station. MCCC: Multi-channel cross-correlation.

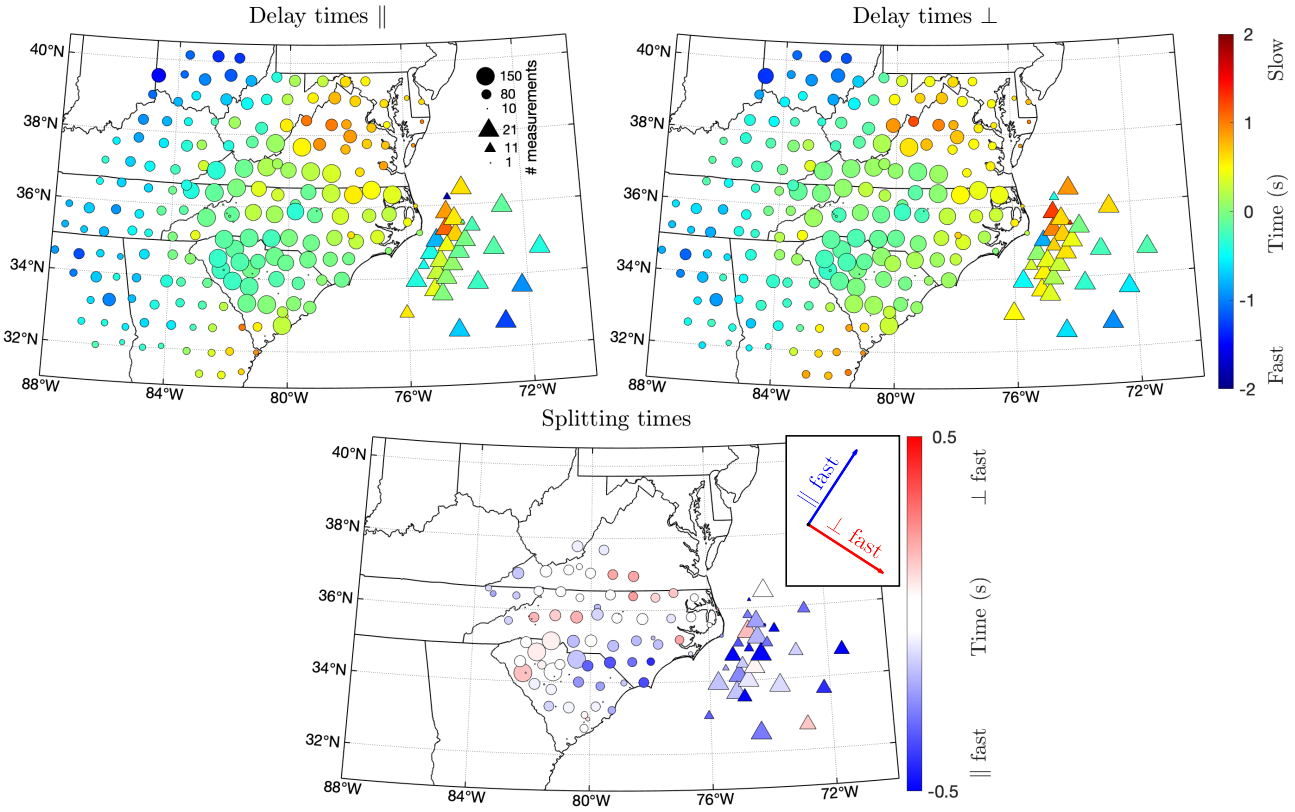

Figure S8. Same as Figure 2, but with results averaged at each station. Times shown are the weighted average of each measurement at a station. The size of a dot represents the number of observations at that station. OBS (plotted as triangles) sizes are multiplied by 8. Sizes are capped between 10 and 150 for clarity. The colorbar for splitting times is capped between -0.5 s and 0.5 s for this figure only.

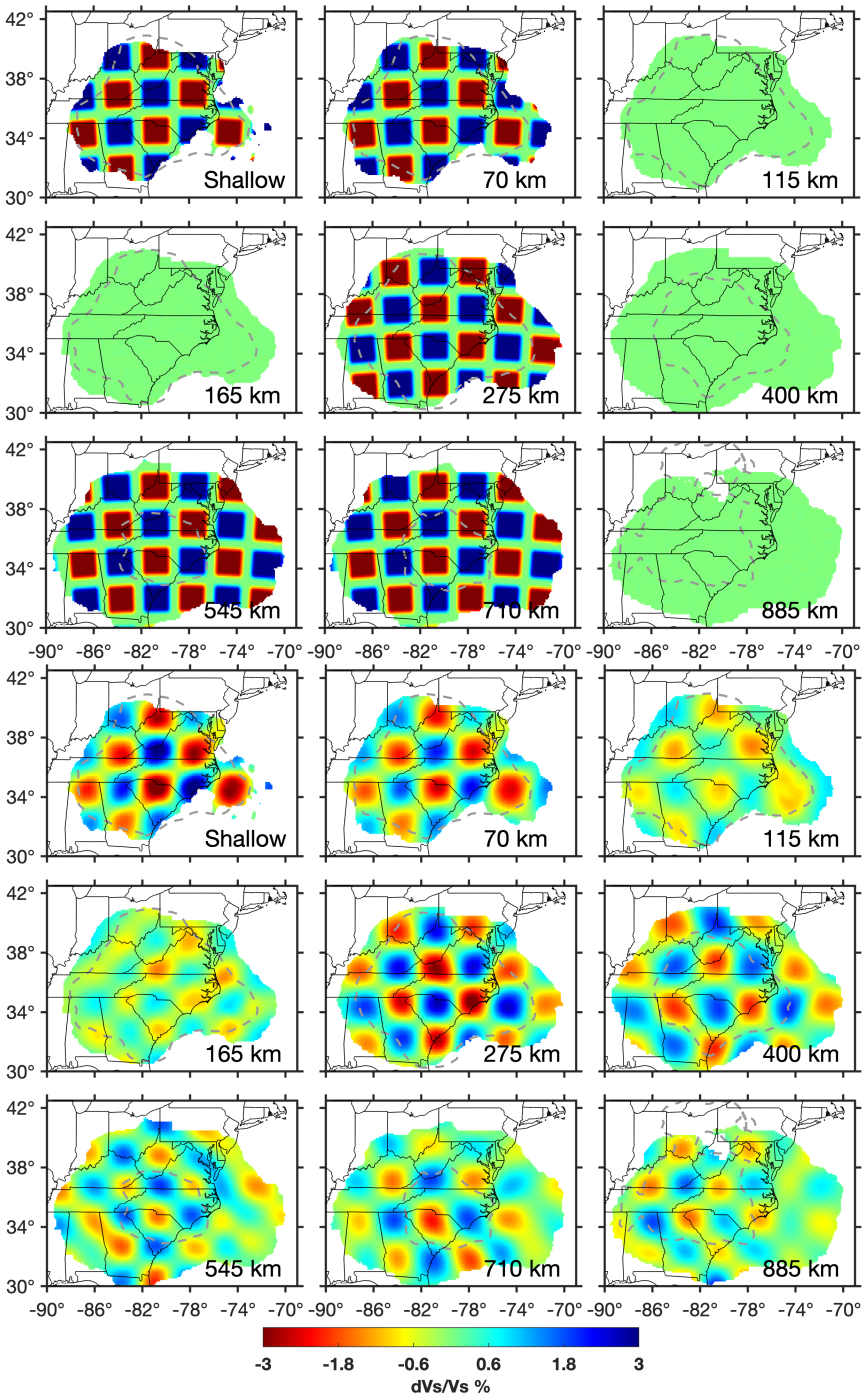

Figure S9. Checkerboard tests for velocity. The top three rows are input and bottom three are output structure. See Figure 3 for more description.

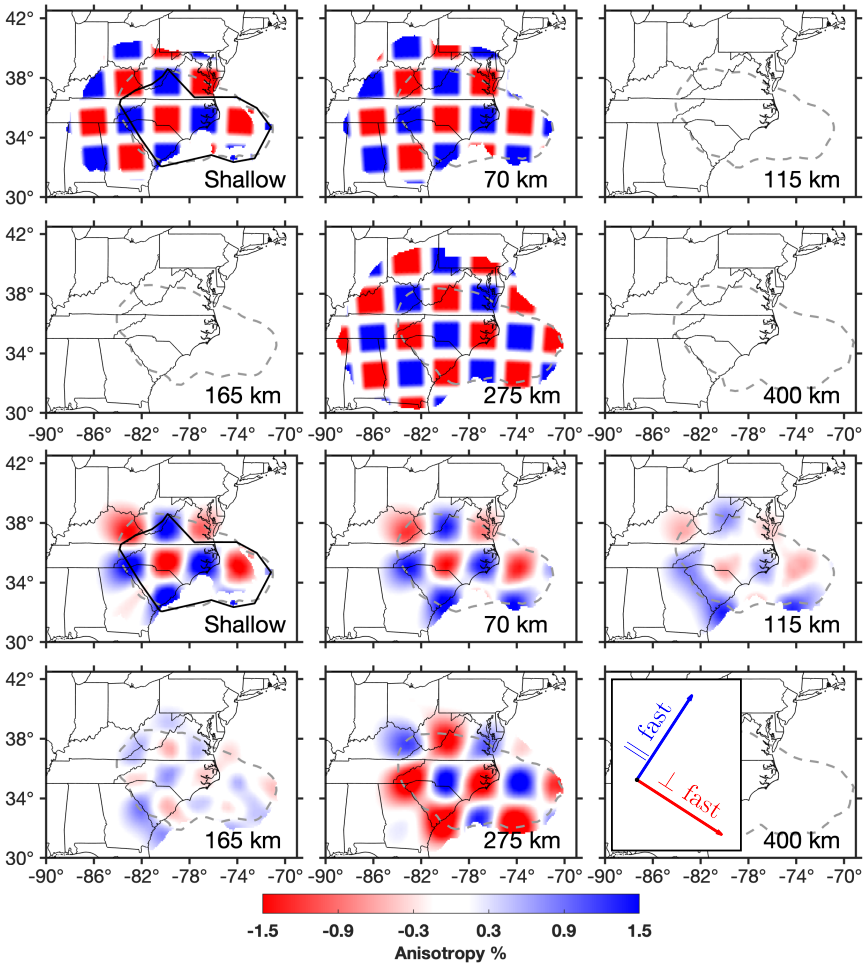

Figure S10. Same as Figure S9, but for anisotropy. See Figure 4 for more description.

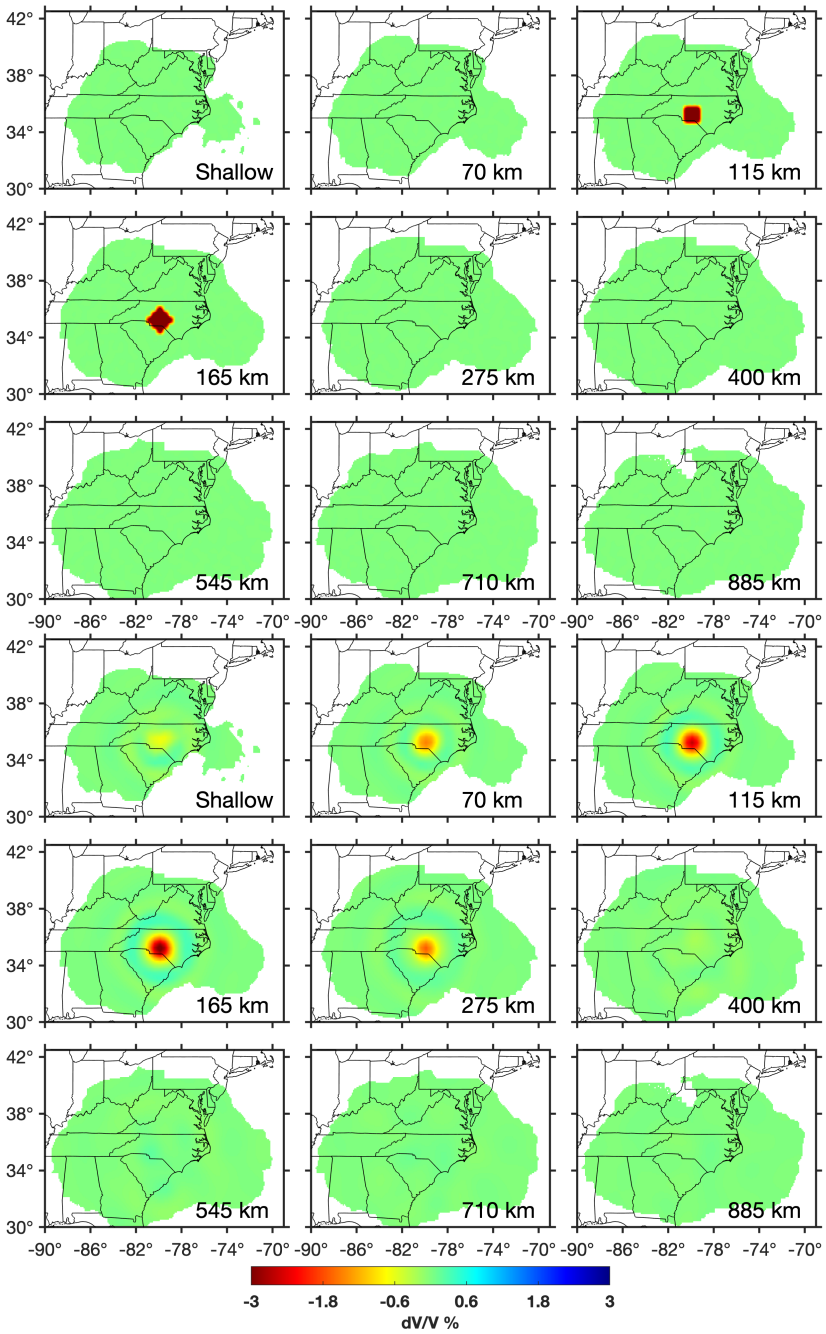

Figure S11. Spike tests using a single spherical spike with a radius of 85 km and center at 165 km depth. Top three rows show input and bottom three rows show output. See Figure 3 for more description.

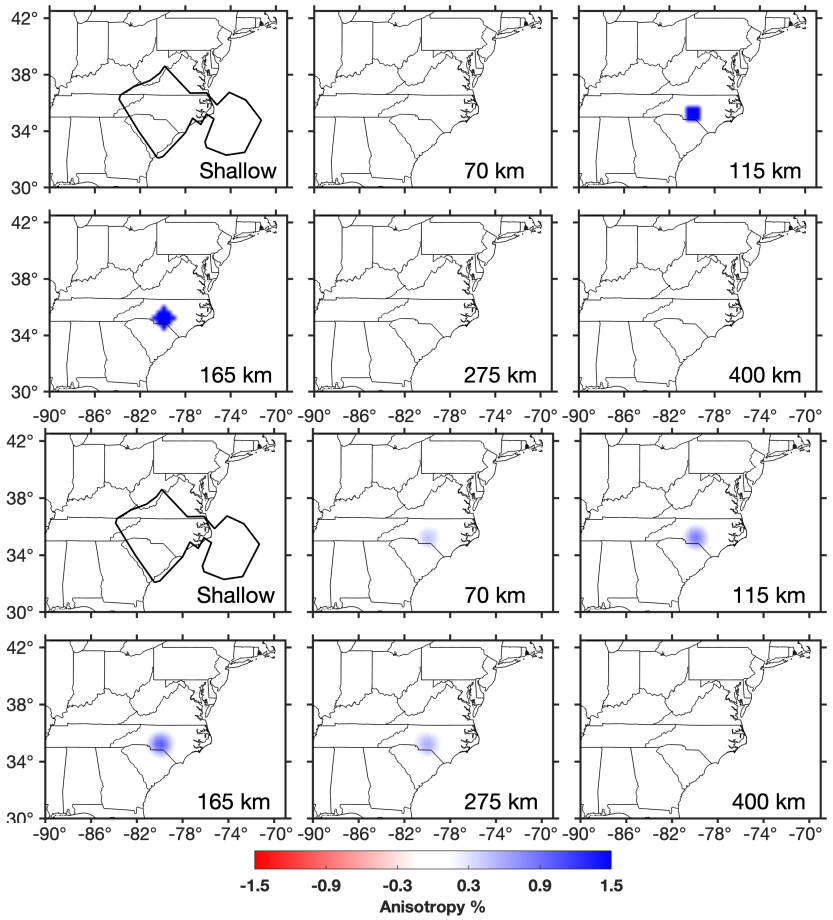

Figure S12. Same as Figure S11, but for anisotropy. Top two rows are input and bottom two rows are output structure. See Figure 4 for more description.

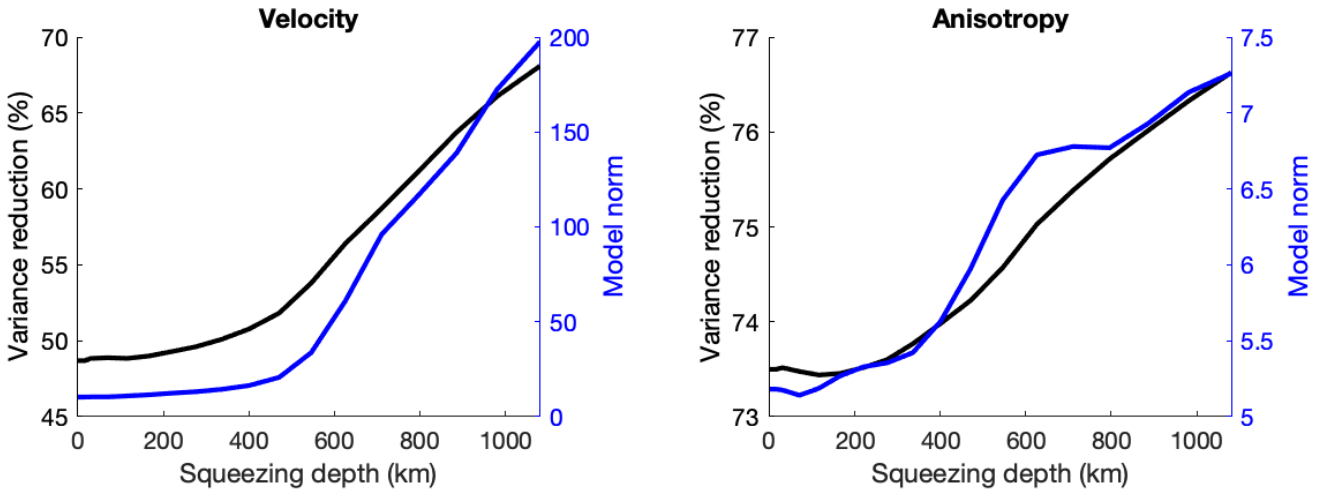

Figure S13. Results of the squeezing test. The squeezing depth z_{sqz} was varied from 0 km to 1080 km. All structure with $z > z_{sqz}$ was assumed to be 0. For each squeezing depth, the resulting model norms for both velocity and anisotropy are shown. The variance reduction of splitting times is shown for the anisotropy figure, while the variance reduction of differential travel times is shown for the velocity figure.

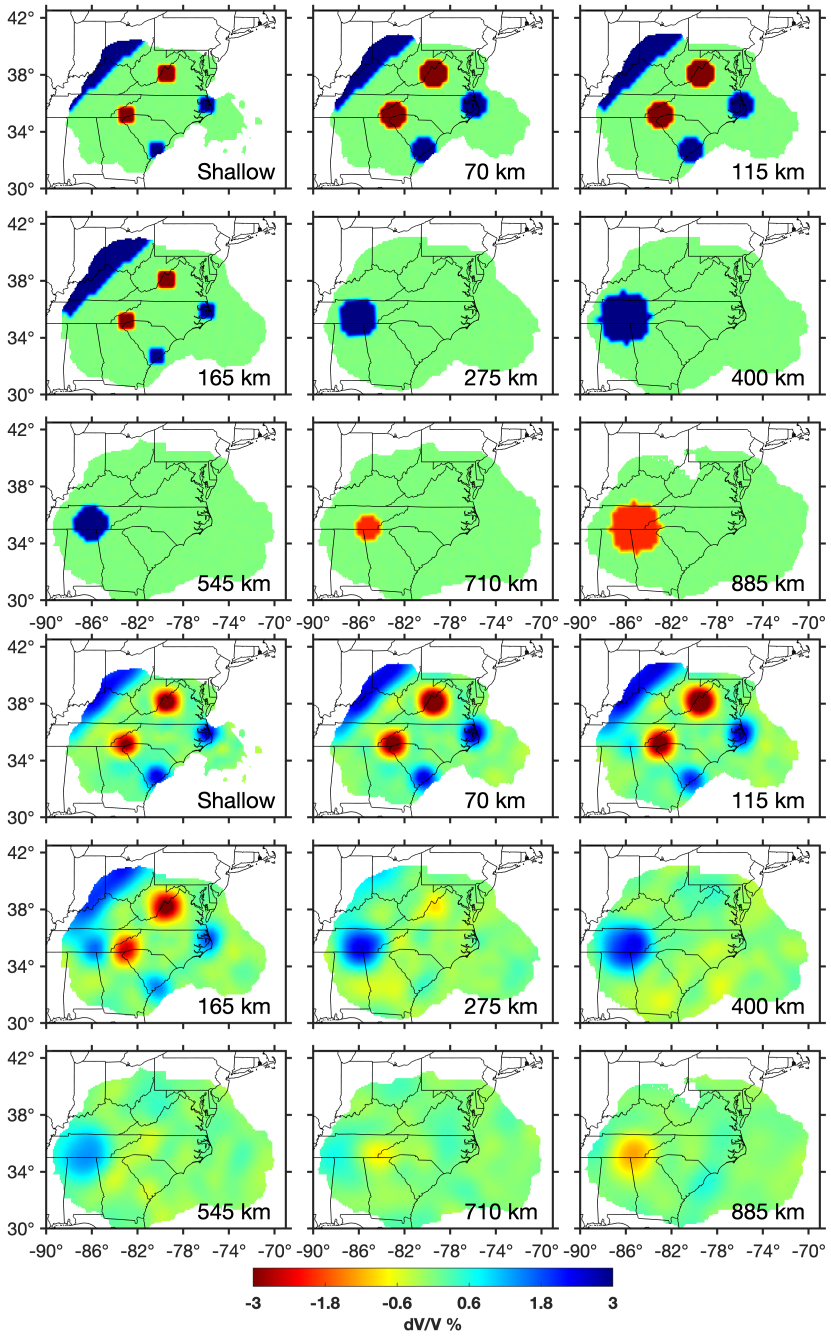

Figure S14. This shows the velocity synthetic input-output tests, where the inputs are chosen to correspond with specific possible observations. Input is top three rows, output is bottom three rows. See Figure 3 for more description.

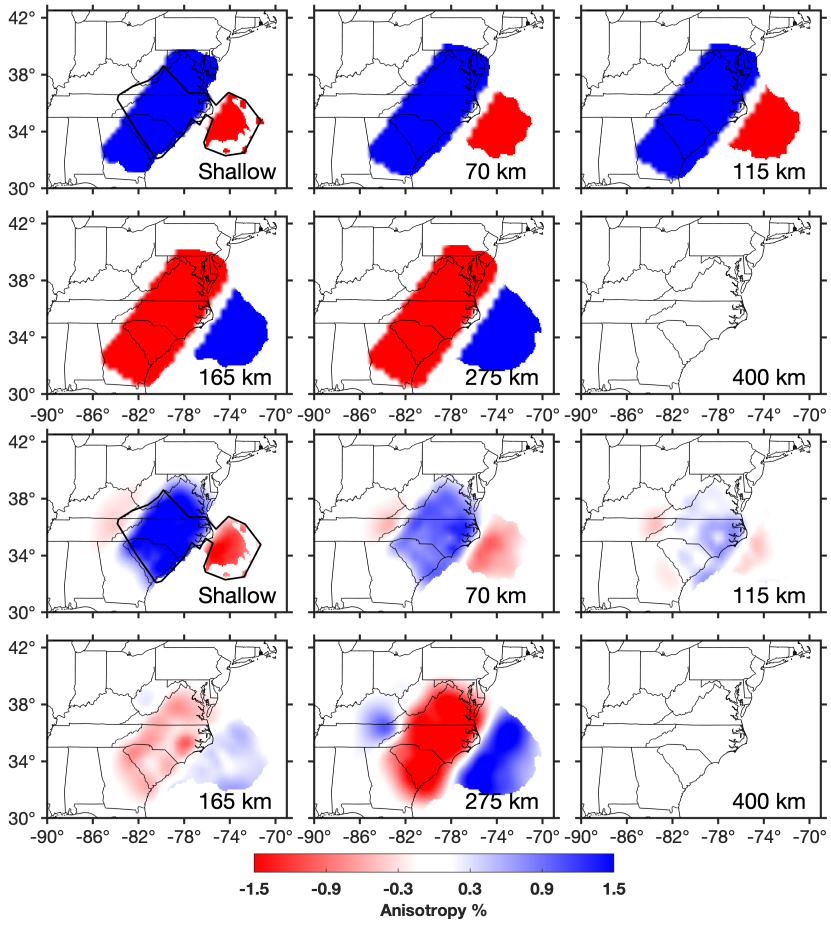

Figure S15. Same as Figure S14, but for anisotropy. See Figure 4 for more description.

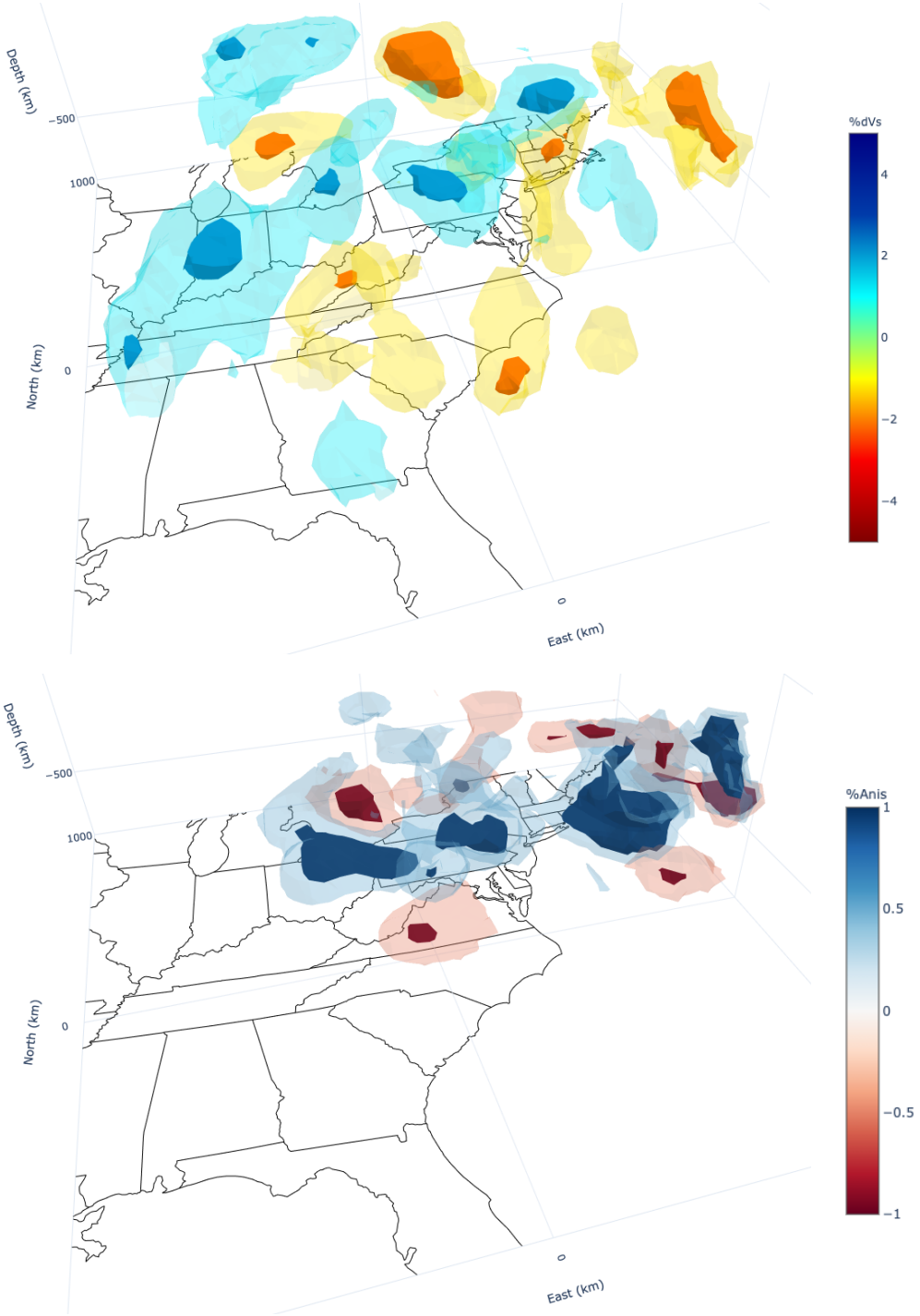

Figure S16. Three-dimensional view of velocity and anisotropy models. dVs isosurfaces are at $\pm 1.2\%, \pm 2.2\%$. Anisotropy isosurfaces are at $\pm 0.5\%, \pm 1.0\%$. Model only plotted where hit quality > 0.7. These files can be viewed interactively using the supplementary file `brunsvik-tomog.html`.